Turning on Visible-Light Photocatalytic C−H Oxidation over Metal−Organic Frameworks by Introducing Metal-to-Cluster Charge Transfer

Caiyun Xu,[†,∥] Yating Pan,[†,∥] Gang Wan,[‡] Hang Liu,[†] Liang Wang,[§] Hua Zhou,[§] Shu-Hong Yu,[†] and Hai-Long Jiang*,[†]

[†]Hefei National Laboratory for Physical Sciences at the Microscale, CAS Key Laboratory of Soft Matter Chemistry, Collaborative Innovation Center of Suzhou Nano Science and Technology, Department of Chemistry, University of Science and Technology of China, Hefei, Anhui 230026, P.R. China

[‡]SLAC National Accelerator Laboratory, 2575 Sand Hill Rd, Menlo Park, California 94025, United States

[§]X-ray Science Division, Advanced Photon Source, Argonne National Laboratory, Lemont, Illinois 60439, United States

S *Supporting Information*

ABSTRACT: The tailorable structure and electronic structure of metal−organic frameworks (MOFs) greatly facilitate their modulated light harvesting, redox power, and consequently photocatalysis. Herein, a representative MOF, UiO-66, was furnished by installing Fe^{3+} onto the Zr-oxo clusters, to give Fe-UiO-66, which features extended visible light harvesting, based on metal-to-cluster charge transfer (MCCT). The Fe-UiO-66 with unique electronic structure and strong oxidizing power exhibits visible light-driven water oxidation, which is impossible for pristine UiO-66. More strikingly, under visible irradiation, the generated holes over Fe-UiO-66 are able to exclusively convert H_2O to hydroxide radicals, initiating and driving the activation of stubborn C-H bond, such as toluene oxidation. The electrons reduce O_2 to $O_2^{•-}$ radicals that further promote the oxidation reaction. The related catalytic mechanism and the structure−activity relationship have been investigated in detail. As far as we know, this is not only an unprecedented report on activating "inert" MOFs for photocatalytic C-H activation but also the first work on extended light harvesting and enhanced photocatalysis for MOFs by introducing an MCCT process.
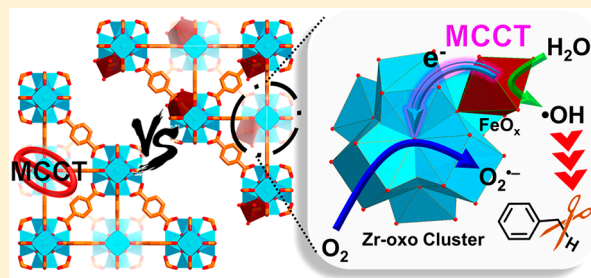
INTRODUCTION

The combustion of hydrocarbon compounds, the major constituent of fossil fuels, has been their main interest while their potential as feedstock for valuable chemicals is largely ignored. Selective oxidation of primary C-H bonds is of great importance to upgrade the primary raw materials.[1−5] Unfortunately, the activation of stubborn C-H bonds (dissociation energy: 440 kJ·mol^{-1}) usually requires harsh conditions, for examples, high temperature and/or high O_2 pressure to generate reactive oxygen species, or the presence of additives with strong oxidation ability (such as hydrogen peroxide, *tert*-butyl hydroperoxide, etc.).[1−5] So far, it remains a great challenge to drive the oxidation of hydrocarbons in the absence of additives under mild conditions. To address this issue, replacing traditional thermocatalysis with photocatalysis might be an effective solution.

As a class of crystalline porous solids, metal−organic frameworks (MOFs) featuring high surface area and tailored pores/structures have captured widespread interest, for their potential applications in diverse fields, such as gas storage/separation, sensors, catalysis, etc.[6−14] Particularly, the linkers in MOFs are able to harvest solar light to generate charge-separated states, which endows MOFs high potential toward photocatalysis.[15−20] MOF-based materials have been demonstrated to be promising photocatalysts for CO_2 reduction, water splitting, organic transformations, and so on.[15−29] However, to the best of our knowledge, photocatalytic oxidation reactions breaking chemically inert bonds (such as C-H bonds) over MOF catalysts under mild conditions (ambient temperature, 1 bar O_2, without additives) has never been reported. To break through this bottleneck, MOFs with wide spectral response and high oxidation potential, particularly sufficient active sites and stable framework structures are prerequisite.[30−32] The metal-to-cluster or metal-to-metal charge transfer (MCCT or MMCT) in inorganic photocatalysts presents an effective strategy to extend light absorbance and guarantee the active sites with proper redox potentials for strong oxidative ability.[33,34] While this MCCT/MMCT process and related strategy would be readily achieved in MOFs thanks to their highly amendable structures, they have never yet been reported.

In this work, we have rationally incorporated Fe^{3+} ions into a representative MOF, UiO-66, by coordinatively binding to the Zr-oxo clusters, resulting in Fe-doped UiO-66 (simply as Fe-UiO-66). The Fe^{3+} introduction induces the MCCT process in MOF, i.e., the charge-transfer from Fe^{3+} to Zr-oxo clusters, which causes extended visible light response. The unique transition of MCCT enables Fe-UiO-66 to catalyze the oxidation of H_2O to hydroxyl radicals (•OH), which possess sufficient oxidizing power to activate C-H bonds (Figure 1). As
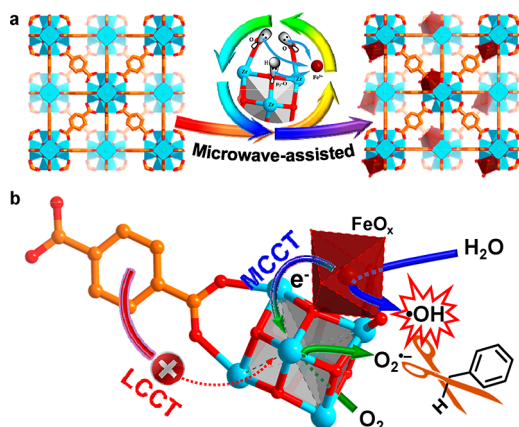
Figure 1. Schematic illustration showing (a) the grafting FeO_x onto the Zr-oxo cluster by coordination interaction, affording Fe-UiO-66, and (b) the conversion of H_2O to •OH by visible-light-driven MCCT process, which is accomplished by the holes on FeO_x, upon electron transfer from FeO_x to Zr-oxo cluster, and the conversion of O_2 to $O_2^{\bullet-}$ based on the accepted electrons on the Zr-oxo clusters. In contrast, the LCCT (ligand-to-cluster charge transfer) process does not occur under visible light irradiation.

a result, by sharp contrast to the completely inert UiO-66, the Fe-UiO-66 with strong oxidation ability exhibits excellent activity and recyclability toward photocatalytic oxidation of hydrocarbons, particularly toluene, with water under ambient temperature, 1 bar O_2, and visible light irradiation.

■ MATERIALS AND METHODS

Materials and Equipments. All chemicals were obtained from commercial sources and were used without further purification otherwise stated. Powder X-ray diffraction patterns were obtained on a Japan Rigaku SmartLab rotating anode X-ray diffractometer (Miniflex 600) equipped with graphite-monochromated Cu $K\alpha$ radiation (λ = 1.54178 Å). UV−vis absorption spectrum was recorded on a Shimadzu UV-2700 spectrophotometer and a white standard of $BaSO_4$ was used as a reference. Gas sorption measurement was conducted by using an automatic volumetric adsorption equipment (Micrometritics ASAP 2020). The transmission electron microscopy (TEM) images were acquired on a JEOL JEM-2100F field-emission transmission electron microscope. The products were analyzed and identified by gas chromatography (Shimadzu GC-2014). The products were further determined by using the Agilent technologies 7890A GC and a mass spectrometer Agilent technologies 5975C as detector. The contents of Fe and Zr in the nanocomposites were quantified by an Optima 7300 DV inductively coupled plasma atomic emission spectrometer (ICP-AES). Field-emission scanning electron microscopy (FE-SEM) was carried out with a field S3 emission scanning electron microanalyzer (Zeiss Supra 40 scanning electron microscope at an acceleration voltage of 5 kV). The X-ray photoelectron spectroscopy (XPS) measurements were performed by using an ESCALAB 250 high performance electron spectrometer using monochromatized Al $K\alpha$ ($h\nu$ = 1486.7 eV) as the excitation source. The photoluminescence was performed by using Perkin-Elmer

LS-55 fluorescence spectrometer. Electron paramagnetic resonance (EPR) spectra were recorded on JEOL JES-FA200 EPR spectrometer under xenon lamp. ^1H NMR and ^{13}C NMR spectra were recorded on a Bruker AC-400FT spectrometer (400 MHz).

The Fe K-edge X-ray absorption spectroscopy measurement was conducted at room temperature in transmission mode at 20-BM beamline in Advanced Photon Source at Argonne National Laboratory. The samples were mixed with boron nitride and pressed to make a pellet before the measurement. The energy calibration, normalization and background removal, and fitting were analyzed using software Athena and Artemis, respectively. The high-energy X-ray diffraction measurement was conducted at the 11-ID-C beamline at the Advanced Photon Source, Argonne National Laboratory with a monochromatic X-ray beam with a size of 0.1×0.1 mm^2 and an energy of 105.74 keV (the corresponding wavelength was 0.11725 Å). A PerkinElmer α-Si flat-panel large-area detector with quadratic pixel size of 200×200 μm^2 was to collect the two-dimensional (2-D) diffraction patterns. The diffraction patterns were calibrated using CeO_2 and then divided into 36 sectors with 10° per sector, using a Fit2D software. Based on the divided diffraction patterns, the structure factor $S(Q)$ was calculated, where Q is the magnitude of scattering factor. The reduced PDF, $G(r)$, was obtained by a Fourier transformation:

$$G(r) = 4\pi r[\rho(r) - \rho_0] = \frac{2}{\pi} \int_0^{Q_{max}} Q(S(Q) - 1) \sin(rQ)\, dQ \tag{1}$$

where $\rho(r)$ and ρ_0 are the local and average atomic number density, and r is the atomic distance. The correction, normalization, calculation of $S(Q)$, and transformation of $S(Q)$ to $G(r)$ were all conducted using the software package of PDFgetX2.

Preparation of UiO-66. Generally, 20 mg of $ZrCl_4$ and 14.25 mg of H_2BDC were dissolved in 10 mL of DMF containing 1.83 mL of HOAc. The mixture was sealed into a 20 mL glass vial and allowed to react at 120 °C for 24 h. The white product was collected by centrifugation and washed with DMF and menthol. After washing, the product was immersed in the methanol to exchange out the DMF, followed by drying under vacuum at 60 °C overnight.

Preparation of Fe-UiO-66. Typically, 40 mg of as-synthesized UiO-66 and 80 mg of $FeCl_3·6H_2O$ were ultrasonically dispersed in 4 mL of MeCN. The mixture was transferred into a 7 mL microwave vessel and sealed. The reaction was then rapidly heated to 85 °C by a microwave reactor (CEM Discover SP) and held at this temperature for 30 min with continuous stirring. After cooling to room temperature, the solid was isolated by centrifugation and washed with H_2O and methanol to remove the excess Fe^{3+}. The synthesized Fe-UiO-66 was obtained by dried at 60 °C under vacuum.

Preparation of MIL-53. Generally, 225 mg of $FeCl_3·6H_2O$ and 138 mg of H_2BDC were dissolved in 16 mL of DMF containing 150 μL of H_2O. The mixture was stirred at room temperature for 1 h, then transferred and sealed into a 20 mL Teflon-line autoclave, and allowed to react at 170 °C for 24 h. The product was collected by centrifugation and washed with the DMF and menthol. After washing, the product was immersed in the methanol to exchange out the DMF, followed by drying under vacuum at 85 °C overnight.

Preparation of UiO-66/MIL-53. Typically, 4.3 mg of MIL-53 and 34 mg of UiO-66 (Fe/UiO-66 = 3 wt%) were mixed and ground for 3 times in an agate mortar using a pestle and then thermally treated at 150 °C for 2 h at vacuum to produce the UiO-66/MIL-53 heterojunction composites.

Photocatalytic O_2 Evolution by Water Oxidation. The photocatalytic O_2 evolution was performed in an online water splitting system (Beijing Perfect Light Technology Co., Ltd.). Typically, 20 mg of catalyst and 200 mg of $AgNO_3$ were dispersed in 30 mL of H_2O. The mixture was transferred into the photoreactor and pumped to extract the dissolved O_2. The circulating water system was used to keep a constant reaction temperature and avoid the solvent evaporation. The reaction proceeded under a pressure of ~-100 kPa in the presence of Xe lamp (LX-300F, Japan) with UV

cutoff filter ($\lambda > 400$ nm). The generated O_2 was quantified by GC equipped with a TCD detector.

Photocatalytic Toluene Oxidation. In a typical experiment, 10 mg of catalyst was dispersed into a 1 mL of MeCN solution containing 20 μL of H_2O and 47.2 μmol of of substrate (5 μL for toluene) and the mixture was transferred into a photoreactor and irradiated by the Xe lamp (LX-300F, Japan) with the UV cutoff filter ($\lambda > 380$ nm). The atmosphere was kept at 1 atm O_2, controlled by a O_2 balloon. The products were analyzed by GC equipped with a FID detector and determined by GC-MS.

For experiments with different toluene concentrations, several certain amounts of toluene were added, while other parameters remain the same, otherwise particularly stated. The rate and TOF value were calculated based on the conversion of 2 h.

For experiments with different types of substrate, 47.2 μmol different substrates were added, while other parameters remain the same, otherwise particularly stated.

For control experiments, a certain amount of additives was added into the mixture, or the reaction atmosphere was replaced, while other parameters remain the same, otherwise particularly stated.

For hot filtration test, the reaction mixture was centrifuged to remove the catalyst. The supernatant was continued to react as the general procedure.

To verify whether the overoxidation of benzoic acid takes place, toluene was replaced by the same molar amount of benzoic acid (1,1,1,2-tetrachloroethan as internal standard), while fixing other parameters. The amount of benzoic acid and products were analyzed by GC equipped with a FID detector and determined by GC-MS, ^{1}H NMR, and ^{13}C NMR spectra.

To examine whether the overoxidation of BDC ligand occurs, the Fe-UiO-66 after catalysis and the fresh UiO-66 (as a control) were dissolved into a NaOH/D_2O mixture. The supernatant as analyzed by ^{13}C NMR spectra.

For isotope tracing experiments, the reactant was replaced with certain isotope labeled reagent, while other parameters remain the same. Small doses of the sample are taken out to detect the progress of the reaction, analyzed by GC-MS. The Mass spectra were collected after the reaction proceeded for 1 h.

EPR Detection of MCCT Process. The EPR measurements were carried out with 1.2 mg of Fe-UiO-66 in 0.2 mL of MeCN/H_2O (10:1) at 140 K under air atmosphere. The result shows that the high-spin Fe^{3+} signal reduces upon light irradiation (500 W Xe lamp, $\lambda =$ 380 nm). Considering the oxidization atmosphere, the formation of Fe(II) can be ignored. It is believed that the formation of the high valence Fe species, such as Fe(IV) at the oxidative end, would be the reason for the decreased Fe^{3+} signal.

To better distinguish the EPR signal of the reduction end, the hole scavenger MeOH was added. The EPR measurements were carried out with 1.2 mg of Fe-UiO-66 in 0.2 mL of MeCN/MeOH/H_2O (5:5:1) at 140 K under N_2 protection. As a result, the signal intensity of oxygen centered active sites in Zr_6-oxo clusters was greatly enhanced in N_2 atmosphere under light irradiation (500 W Xe lamp, $\lambda =$ 365 nm). Once air was in situ introduced, this signal was reduced significantly, indicating the electron transfer from Fe to Zr-oxo and then to O_2 (from air). The control experiments, performed by replacing Fe-UiO-66 with UiO-66 only, gave no difference before and after illumination, further revealing the visible-light response from MCCT in Fe-UiO-66.

EPR Detection of Reactive Oxygen Species. For detection of $O_2^{\bullet-}$ radical, the EPR measurements were carried out with 3.0 mg of Fe-UiO-66 in 0.5 mL of MeOH at 140 K under air atmosphere. The DMPO was added as the radical trapping agent and MeOH was employed as hole scavenger to reduce the interference from hydroxyl radical.[35] The Xe lamp equipped with single wavelength filter (500 W Xe lamp, $\lambda =$ 380 nm) was used as light source.

For detection of $\bullet$OH radical, EPR measurements were carried out with 1.2 mg of Fe-UiO-66 in 0.2 mL of MeCN/H_2O/$AgNO_3$ (4:4:1) at 140 K under air atmosphere in the beginning. The DMPO was added as the radical trapping agent and $AgNO_3$ was employed as electron scavenger to reduce the interference from $O_2^{\bullet-}$. The Xe lamp

equipped with single wavelength filter (500 W Xe lamp, $\lambda =$ 380 nm) was used as light source. Since the generated $\bullet$OH radical can decompose the organic solvent, some interfering substances were generated during the test, such as $^\bullet$DMPO-CH_3. To get better signal of DMPO-$\bullet$OH,[36] EPR measurements were also carried out with 1.2 mg of Fe-UiO-66 in 0.2 mL of H_2O at 140 K under air atmosphere (500 W Xe lamp, $\lambda =$ 380 nm).

Photoelectrochemical Measurements. Photocurrent measurements were performed on a CHI 760E electrochemical work station (Chenhua Instrument, Shanghai, China) in a standard three-electrode system with the photocatalyst-coated ITO as the working electrode, Pt plate as the counter electrode, and an Ag/AgCl as a reference electrode. A 300 W xenon lamp with cutoff filter ($\lambda > 400$ nm) was used as light source. A 0.1 M Na_2SO_4 solution was used as electrolyte. The catalyst (3 mg) was added into a mixed solution with 10 μL of 5 wt% Nafion and 2 mL of ethanol, and the working electrodes were prepared by dropping the suspension (200 μL) onto the surface of a ITO plate with an area of 4 cm^2. The working electrodes were dried, and the photoresponsive signals of the samples were measured under chopped light at + 0.5 V.

Mott−Schottky plots and electrochemical impedance spectroscopy (EIS) of UiO-66 or Fe-UiO-66 were measured on an electrochemical workstation (Zahner Zennium) in a standard three-electrode system with the photocatalyst-coated glassy carbon ($\Phi =$ 3 cm) as working electrode, Pt plate as counter electrode, and Ag/AgCl as reference electrode. A 0.1 M Na_2SO_4 solution after deoxidation was used as the electrolyte. The catalyst (3 mg) was added into 10 μL of 5 wt% Nafion and 2 mL of ethanol mixed solution, and the working electrode was prepared by dropping the suspension (30 μL) onto the surface of the glassy carbon electrode. Mott−Schottky plots were taken at frequencies of 500, 1000, and 1500 Hz, respectively. EIS was carried out with a bias of −1.5 V.

Detection of $\bullet$OH by a Fluorescent Method. Small molecule terephthalic acids react with $\bullet$OH radicals to generate fluorescent products, which can be used to detect the generation of $\bullet$OH.[37] Typically, 10 mg of catalyst and 10 mg of terephthalic acid were dispersed in 10 mL of MeCN containing 1 mL of borax buffer (pH 9, 0.1 M). The mixture was transferred into a two-neck flask, with an O_2 balloon to keep the system at 1 atm O_2 atmosphere. The light source was Xe lamp with the UV cutoff filter ($\lambda > 380$ nm). After reaction, 1 mL of the reaction mixture was extracted and diluted by 3 mL of H_2O every 30 min. The resulting fluorescence was detected by the Perkin-Elmer LS-55 fluorescence spectrometer.

■ RESULTS AND DISCUSSION

The incorporation of Fe^{3+} into UiO-66 was accomplished by microwave-assisted modification. The Fe loading of 2.97 wt% was decided by ICP-AES, indicating that $\sim$1.2 Fe atoms furnished onto per Zr_6-oxo cluster. The high crystallinity of UiO-66 is maintained after Fe^{3+} modification, as evidenced by the powder X-ray diffraction (XRD) profile (Figure S1). The introduction of Fe^{3+} does not disturb the original octahedral morphology of UiO-66 and no extra particles can be observed inside/outside Fe-UiO-66, as shown in scanning electron microscope (SEM) and transmission electron microscope (TEM) images (Figures 2a,b and S2). Nitrogen sorption isotherms indicate the adsorption capacity of Fe-UiO-66 is slightly lower than that of UiO-66, possibly due to the mass occupation of additional Fe^{3+} ions (Figures 2c and S3).
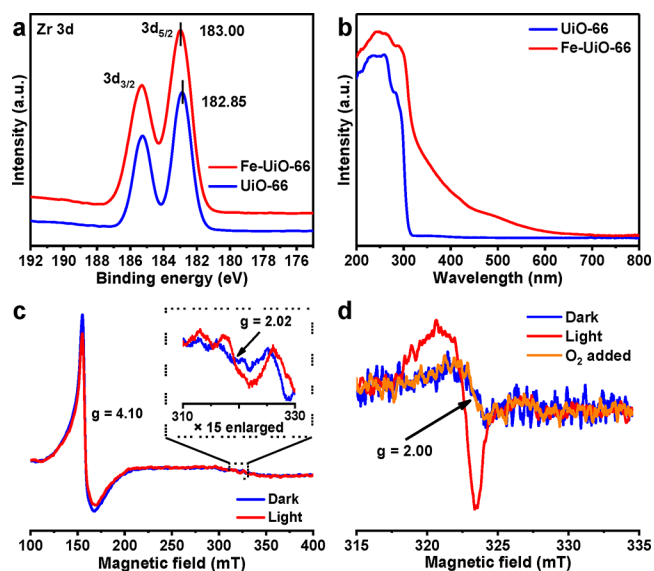
The chemical environment of Fe-UiO-66 catalyst has been investigated by X-ray absorption spectroscopy (XAS) and pair distribution function (PDF). In the Fe K-edge X-ray absorption near-edge structure (XANES) spectra, the absorption threshold is very close to Fe_2O_3, indicating the existence of an oxidation state of +3 for Fe species (Figure 2d). In the Fourier-transformed extended X-ray absorption fine structure (FT-EXAFS) spectra, there is a dominant peak
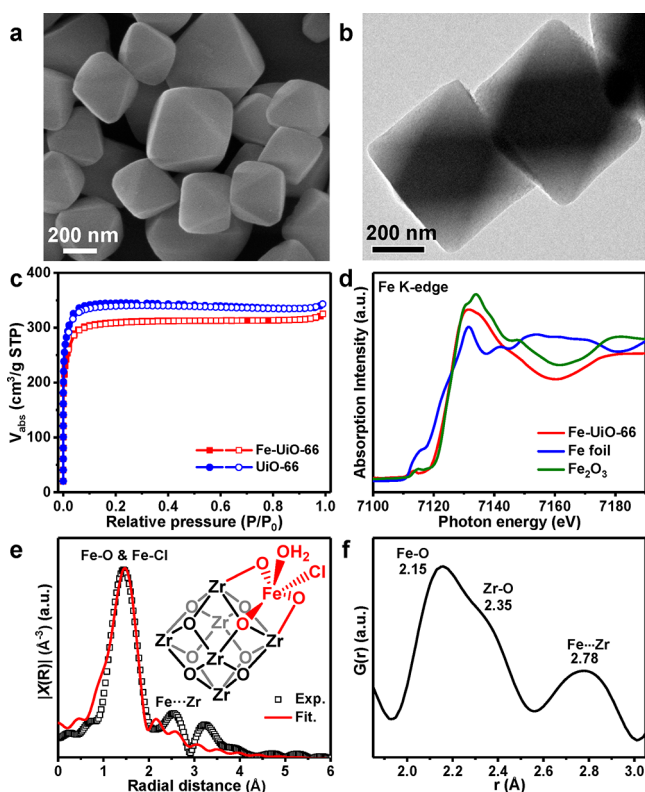
Figure 2. (a) SEM and (b) TEM images of Fe-UiO-66. (c) N_2 sorption isotherms (solid: adsorption curve; open: desorption curve) of UiO-66 and Fe-UiO-66 at 77 K. (d) Fe K-edge XANES of Fe-UiO-66, Fe foil, and Fe_2O_3. (e) FT-EXAFS and its fitting curve (inset: proposed structure of Fe-modified Zr-oxo cluster) of Fe-UiO-66. (f) Atomic PDF analysis for Fe-UiO-66.

Figure 3. (a) Zr 3d XPS and (b) UV−vis spectra of UiO-66 and Fe-UiO-66. EPR spectra of Fe-UiO-66 for the detection of (c) Fe state change before and after illumination in air, and (d) electron transfer before and after illumination in N_2.

located at 1.47 Å, with an absence of Fe-Fe bond at 2.13 Å (Fe foil) or 2.57 Å (Fe_2O_3; Figure S4). The first-shell coordination environment around Fe centers can be ascribed to Fe-O/Cl bonding, and fitting of FT-EXAFS gives the average coordination number of 5 and bonding distance of 2.10 Å, which accord with the proposed cluster structure (Figures 2e and Table S1).[9,38−40] To further identify the proposed structure, atomic PDF analysis has been conducted and gives bond lengths of 2.15 Å and 2.35 Å (Figure 2f),[41,42] in line with the Fe-O and Zr-O bonds, respectively. The peak at 2.78 Å can be assigned to Fe⋯Zr bonds connected by oxygen bridge. The chemical states of Fe and Zr in UiO-66 and Fe-UiO-66 were further examined by using X-ray photoelectron spectroscopy (XPS). Upon introducing Fe species into UiO-66, the Fe $2p_{3/2}$ binding energy of 711.4 eV verifies the Fe(III) state (Figure S5), and the peak of Zr $3d_{5/2}$ shifts to higher binding energy from 182.85 to 183.00 eV (Figure 3a). Given the stronger electron withdrawing capability of Fe(III) than proton, this shift is reasonable upon the formation of Zr(IV)-O-Fe(III) in Fe-UiO-66. The above data together unambiguously demonstrate that the introduced Fe^{3+} ions sit on the Zr-oxo cluster via the Fe-O-Zr connection in Fe-UiO-66 (Figure 2e, inset).

The influence of Fe^{3+} introduction on the electronic structure of UiO-66 has been examined. UV−vis absorption spectra indicate that the intrinsic absorption edge of UiO-66 shows a red-shift upon Fe^{3+} modification, extending the light absorption to visible region (Figures 3b and S6).[33,34] The band structure of the resulting Fe-UiO-66 was investigated to evaluate its oxidizing power. Apparently, the Mott−Schottky

plots of UiO-66 and Fe-UiO-66 at various frequencies disclose their typical *n*-type characteristics of semiconductor, owing to the positive slope of the linear plots (Figure S7). The flat band positions referring to the lowest unoccupied molecular orbital (LUMO) in UiO-66 and Fe-UiO-66 are determined from the intersection with value of −0.86 and −0.61 V vs Ag/AgCl (i.e., −0.66 and −0.41 V vs NHE).[23] Based on the band gaps estimated by Tauc plots (Figure S8), the overall energy diagrams can be drawn. The introduction of Fe^{3+} lowers the LUMO energy level and markedly lifts the HOMO energy level of pristine UiO-66, according to the energy level diagrams (Figure S7, insets). Theoretically, they both have the feasibility for the water oxidation ($E_{\bullet OH/OH^-}$ = 1.89 V vs NHE; E_{O_2/H_2O} = 1.23 V vs NHE).[43]

In situ electron paramagnetic resonance (EPR) results under light irradiation unveiled the electron transfer mechanism. The EPR peak at g = 4.10, which is ascribed to high-spin Fe(III),[44,45] shows evident decrease after light irradiation, accompanying with the appearance of a new peak at g = 2.02 assignable to the reduction product of $O_2^{\bullet-}$ adsorbed onto Zr-oxo clusters (Figure 3c).[46−48] As the experiment was conducted in oxidative atmosphere (for example, O_2), the original Fe(III) is supposed to be oxidized to a higher oxidation state, which does not give EPR signals, rather than being reduced to a lower oxidation state. Upon the addition of methanol as a hole sacrificial agent, the signal (g = 2.00) of oxygen centered active sites in Zr-oxo clusters emerges upon accepting electrons from Fe(III), can be evidently observed in N_2 atmosphere under light irradiation (Figure 3d), in sharp contrast to no signal by UiO-66 (Figure S9), demonstrating the electron acceptor behavior of Zr-oxo clusters in Fe-UiO-66.[17,46−48] Once air is introduced, this signal (g = 2.00) is significantly reduced, suggesting the electron transfer from the Zr-oxo cluster to O_2 as the electron acceptor.[46−48] Based on the above in situ EPR results, electron transfer from Fe^{3+} to Zr-oxo clusters, i.e., MCCT process, can be safely assumed.[33,34] The extended light absorption in visible region in Fe-UiO-66 might be attributed to the MCCT process (Figure 3b). Further

photocurrent response under visible light and electrochemical impedance spectroscopy (EIS) tests also indicate much enhanced charge separation efficiency of Fe-UiO-66, in reference to UiO-66 (Figure S10). It should be stated that, the introduced second metal (Fe) to M-oxo clusters herein serves more likely as electron donors and oxidation sites, rather than electron mediators to improve charge separation,[49,50] under illumination.

The tailored electronic structure by Fe introduction, as indicated above, gives rise to significant influence on the resultant photocatalytic activity. In photocatalytic water splitting system over Fe-UiO-66, in the presence of $AgNO_3$ as an electronic sacrificial agent, the O_2 is vividly produced along with time and the activity reaches 246 $\mu mol \cdot g^{-1} \cdot h^{-1}$ under visible light irradiation ($\lambda > 400$ nm). By sharp contrast, UiO-66 shows negligible activity under the same conditions (Figure S11).

Given the lower value-added nature of O_2 than its intermediate hydroxyl radicals, it would be more valuable to oxidize water to hydroxyl radicals, which might drive strong oxidation reactions of organics, for example, selective oxidation of hydrocarbons. Toluene oxidation was chosen as a representative and carried out at ambient temperature, 1 atm O_2 atmosphere under visible light (Table 1). To our delight, the reaction gives 70.1% toluene conversion in the first 2 h and finally 96.9% conversion with nearly complete selectivity to benzoic acid at 3.5 h over Fe-UiO-66 (entry 1 and Figure S12). Hot filtration experiment demonstrates that the oxidation catalysis occurs heterogeneously (Figure S13). Though

benzoic acid is able to undergo mineralization with ●OH radicals, the mineralization is negligible or very slow in our catalytic system (Figure S14).

The stability of the catalyst has been examined by multiple characterizations. The framework's stability was confirmed by powder XRD and ^{13}C NMR (Figure S15), of which the ligand (BDC) does not undergo hydroxylation by ●OH. The SEM and TEM images prove that morphology of Fe-UiO-66 is retained and no apparent heterogeneous particle appears within the MOF particle, indicating the absence of iron agglomeration (Figure S2). The ICP-AES results indicate a very few iron leaching (0.03 wt% of catalyst), which may be the detachment of iron from the Zr_6 cluster. Moreover, the reusability of Fe-UiO-66 can be well maintained in at least five consecutive runs (Figures S16).

The reaction scaling up and substrate extension have been investigated to broaden the reaction applicability. Along with increased substrate concentration, enhanced activity can be achieved (Figure S17), exhibiting a record-high activity toward the photocatalytic selective toluene oxidation (Table S2). By optimizing the reaction conditions, the selectivity (100%) toward benzaldehyde can be obtained with a 12.6% conversion in a scaling up catalytic reaction (Figure S18). Moreover, such oxidation of C-H bonds over Fe-UiO-66 can be extended to diverse substrates, such as the substituted toluenes (Table S3) and alkylbenzenes (Figure S19, Table S4) as well as benzyl alcohol (Figure S20).

To examine the prerequisites of toluene oxidation by Fe-UiO-66, diverse control experiments have been conducted. As the oxygen content in reaction atmosphere decreases, the catalytic activity decreases significantly (entries 2, 3), high-lighting the crucial role of O_2. The replacement of light source with heating at 60 °C does not give any conversion (entry 4), suggesting the photodriven catalytic process. The removal of water, being assumed as one of the reactants, from the reaction system leads to the significantly reduced activity (entry 5). To rule out the possible formation of Fe_2O_3 or MIL-53 during the synthesis, all UiO-66, Fe_2O_3, their physical mixtures, MIL-53 and UiO-66/MIL-53 heterojunction are examined, failing to give any observable activity (entry 6−10, Figure S21). Therefore, all oxygen gas, light irradiation, water, and MCCT process are indispensable toward this catalytic oxidation conversion.

Quenching experiments have been performed to recognize the reactive oxygen species contributing to the catalysis. The NH_2-UiO-66, a classical catalyst capable of producing $O_2^{\bullet-}$,[46−48] has no activity under visible light irradiation (entry 11), indicating that the generated $O_2^{\bullet-}$ cannot initiate the reaction. The H_2O_2 addition gives a low conversion of 20.3%, implying that the high activity of this reaction does not caused by Fenton reaction of H_2O_2 (entry 12). The introduction of 2-methylfuran as a $^1O_2$ quencher almost does not affect the activity, illustrating that $^1O_2$ is not responsible for the activity (entry 13). The addition of electron scavenger results in significantly increased conversion (entry 14), implying that the formation of key intermediates is driven by hole oxidation. This assumption has been further confirmed by introducing the sacrificial electron donor trimethylamine (TEA), which completely prevents the reaction (entry 15). As a further demonstration, the addition of ●OH radical capturing agent TEMPO almost completely quenches the activity (entry 16), suggesting that the hydroxyl radical

**Table 1. Toluene Oxidation under Different Conditions**[a]

entry	catalyst	atm.	t/h	c.[b]	sel.[b](A/B/C)
1	Fe-UiO-66	O_2	2	70.1	6.4/19.3/74.3
			3.5	96.9	0/3.1/96.7
2	Fe-UiO-66	Air	2	24.6	3.8/25.0/71.2
3	Fe-UiO-66	N_2	2	8.9	25.0/75.0/0
			4	17.8	10.8/78.6/11.2
4[c]	Fe-UiO-66	O_2	2	0	
5[d]	Fe-UiO-66	O_2	2	2.2	0/100/0
6	UiO-66	O_2	2	0	
7	Fe_2O_3	O_2	2	0	
8[e]	UiO-66 + Fe_2O_3	O_2	2	0	
9	MIL-53	O_2	2	0	
10[e]	UiO-66/MIL-53	O_2	2	0	
11	NH_2-UiO-66	O_2	2	0	
12[f]	Fe-UiO-66	O_2	2	20.3	0/79.1/20.8
13[g]	Fe-UiO-66	O_2	2	67.8	7.8/31.7/70.5
14[h]	Fe-UiO-66	O_2	2	100	0/78.0/22.0
15[i]	Fe-UiO-66	O_2	2	0	
16[j]	Fe-UiO-66	O_2	2	0.3	0/35.3/64.7

[a]Reaction conditions: 5 μL toluene, 1 mL MeCN, 10 mg catalyst, 20 μL H_2O, 300 W Xe Lamp with a UV cut ($\lambda > 380$ nm), 1 atm O_2. [b]Determined by GC/GC-MS. [c]At 60 °C, without light. [d]Without introducing water. [e]The Fe content is fixed to the same. [f]Replacing 20 μL of H_2O with 4.7 μL of 30% H_2O_2. [g]Additive: 20 mM 2-methylfuran as $^1O_2$ quencher. [h]Additive: 20 mM $(NH_4)_2Ce(NO_3)_6$ as sacrificial electron donor. [i]Additive: 20 mM TEA as hole sacrificial agent. [j]Additive: 100 mM TEMPO as ●OH capturing agent.

generated by the hole oxidation should be the key intermediate.

We have further proved the reactive oxygen species by EPR experiments. To avoid the interference by •OH radicals, $O_2^{•-}$ was examined in the MeOH solvent instead of pure H_2O. The generation of $O_2^{•-}$ can be detected in air, where the broadening of the EPR signal peak is due to the MeOH solvent (Figure S22).[35,37] Moreover, the generation of •OH radicals has also been evidenced by the in situ EPR tests in different solvents (Figure S23). The above results imply that O_2 molecules accept photogenerated electrons to produce $O_2^{•-}$ radicals and the holes oxidize water to generate •OH radicals under the photocatalytic conditions (Figure 4). To verify whether the
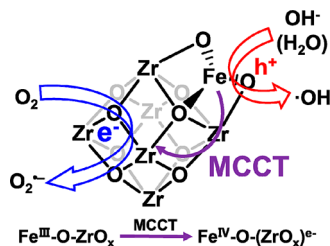
Figure 4. Proposed the photocatalytic generation of $O_2^{•-}$ and •OH radicals over Fe-UiO-66 based on the MCCT process.

origin of •OH radicals is from water oxidation or/and the decomposition of H_2O_2 that is possibly produced via the O_2 reduction, terephthalic acid (TPA) is used as an indicator to evaluate the formation rate of •OH by means of fluorescence method.[37,51] Regardless of the N_2 or O_2 atmosphere, the formation rate of •OH radicals shows almost no difference (Figure S24), suggesting that the generation of •OH is mainly originated from water oxidation by the holes.[51]

To gain insight into the relationship between the active species and the catalytic procedure, systematic isotope tracing experiments have been conducted.[52−55] The control experiments with d_8-toluene give kinetic isotope effect (KIE, k_H/k_D) value of 2.1, which suggests that the C-H bond cleavage in toluene is involved in the catalytic procedure (Figures S25 and S26). In the isotope experiment of $H_2^{18}O$, it can be found that the reaction is significantly inhibited with k_{16O}/k_{18O} of 2.3, which means the primary kinetic isotope effect (PKIE) and O-H cleavage is involved in the rate-determining step (Figure S27).[52,53] The 63.7% ^{16}O in benzaldehyde products replaced by ^{18}O support the participation of •OH radicals (Figure 5a), which are from $H_2^{18}O$ as demonstrated above. A small percentage of ^{18}O are involved in both hydroxyl and carbonyl groups of benzoic acid product (Figure 5b), supporting that •OH radicals participate in the final oxidation process. Compared with benzaldehyde, the proportion of ^{18}O decreases (from 63.7% to 34.0%) in final benzoic acid products (Figure 5b), indicating the O_2 participation in benzaldehyde oxidation to benzoic acid.[54] In the isotope experiment of $^{18}O_2$, the rather low KIE value (k_{16O}/k_{18O}) of 1.3 means O_2 makes less influence than H_2O (Figure S28). The ^{18}O proportion in resultant benzoic acid (51.4%) is much higher than that in benzaldehyde (11.4%), implying the O_2 participates more than H_2O in the benzaldehyde oxidation (Figure S29). In the subsequent kinetic experiments of D_2O, the KIE value (k_H/k_D) of 3.1 further indicates that water oxidation (O-H cleavage) forming •OH radicals is the rate-determining step during the toluene oxidation (Figure S30), in agreement with the above
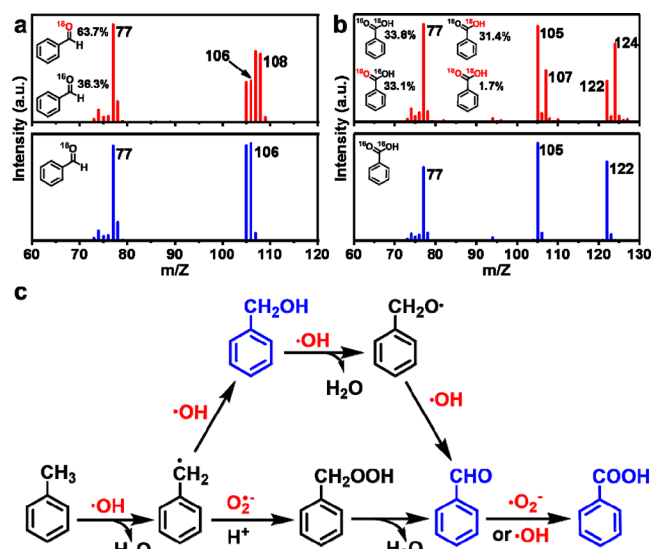
Figure 5. Mass spectra of the obtained (a) benzaldehyde and (b) benzoic acid in the isotope tracing experiments of $H_2^{18}O$. The blue lines were mass spectra of the corresponding standards. The proportions of the isotope labeled products are marked in the figure, calculated by the intensity of fragment peaks. (c) Proposed catalytic mechanism of toluene oxidation over Fe-UiO-66.

$H_2^{18}O$ isotope experiment. The appearance of deuterium in benzyl alcohol demonstrates that •OH is also involved in the formation of alcohol products (Figure S31).

Based on the above experimental results, we reach the reaction mechanism of toluene oxidation over Fe-UiO-66.[56,57] When Fe-UiO-66 is photoexcited under visible light irradiation, electrons from Fe^{3+} migrate along the oxygen bridge to Zr-oxo cluster, forming the charge separation state (Figure 4). Photogenerated electrons can reduce O_2 to $O_2^{•-}$ radicals and the corresponding holes oxidize H_2O to •OH radicals, both of which are active species in the toluene oxidation (Figure 5c). The •OH radicals are believed to play the decisive role to initiate the reaction and first make toluene dehydrogenate to form benzyl radicals,[57] which is different from the direct C-H activation by hole.[5] The $O_2^{•-}$ alone is not able to initiate the catalytic reaction, as evidenced by the inactive NH_2-UiO-66 (entry 11). Benzyl radicals accept •OH to produce benzyl alcohol and subsequent benzaldehyde. In addition, benzyl radicals can be also oxidized by $O_2^{•-}$, with the help of protons, followed by dehydration to give benzaldehyde.[57] With •OH or/and $O_2^{•-}$ radicals, the benzaldehyde can be further oxidized to benzoic acid in the end. Evidenced by the control experiments of benzyl alcohol and benzaldehyde oxidations (Figure S20), the whole reaction is believed to be a relay mechanism, which can help to control the product distribution.

■ CONCLUSIONS

In summary, we have facilely furnished Zr-oxo cluster with Fe^{3+} in UiO-66 to give Fe-UiO-66 by a microwave-assisted approach. The fine structure involving Fe-O-Zr connection has been jointly demonstrated by XAS and PDF results. The Fe^{3+} introduction gives rise to metal-to-cluster charge transfer (MCCT) that extends light absorbance of pristine UiO-66 to visible region. Accordingly, under visible light irradiation, the electrons migrate from Fe^{3+} to Zr-oxo clusters to form the charge separated state and thus enable redox reactions.

Photogenerated holes oxidize water to ●OH radicals, the latter of which are able to initiate and drive the harsh C-H oxidation reactions, such as toluene oxidation. The electrons reduce O_2 to $O_2^{•-}$ radicals that further promote this oxidation process. To the best of our knowledge, this is the first report on extending light harvesting and boosting photocatalysis simultaneously for MOFs *via* an MCCT process. The photoinduced MCCT process developed herein would open an avenue to visible light photocatalysis using MOFs toward diverse reactions.

■ ASSOCIATED CONTENT

Ⓢ Supporting Information

The Supporting Information is available free of charge at https://pubs.acs.org/doi/10.1021/jacs.9b09954.

Additional figures as mentioned in the text (PDF)

■ AUTHOR INFORMATION

Corresponding Author

*jianglab@ustc.edu.cn

ORCID Ⓞ

Shu-Hong Yu: 0000-0003-3732-1011

Hai-Long Jiang: 0000-0002-2975-7977

Author Contributions

‖C.X. and Y.P. contributed equally.

Notes

The authors declare no competing financial interest.

■ REFERENCES

(1) Bergman, R. G. C-H Activation. *Nature* **2007**, *446*, 391−393.

(2) Kesavan, L.; Tiruvalam, R.; Ab Rahim, M. H.; bin Saiman, M. I.; Enache, D. I.; Jenkins, R. L.; Dimitratos, N.; Lopez-Sanchez, J. A.; Taylor, S. H.; Knight, D. W.; Kiely, C. J.; Hutchings, G. J. Solvent-Free Oxidation of Primary Carbon-Hydrogen Bonds in Toluene Using Au-Pd Alloy Nanoparticles. *Science* **2011**, *331*, 195−199.

(3) Ravi, M.; Ranocchiari, M.; van Bokhoven, J. A. The Direct Catalytic Oxidation of Methane to Methanol-A Critical Assessment. *Angew. Chem., Int. Ed.* **2017**, *56*, 16464−16483.

(4) Long, J.; Liu, H.; Wu, S.; Liao, S.; Li, Y. Selective Oxidation of Saturated Hydrocarbons Using Au-Pd Alloy Nanoparticles Supported on Metal-Organic Frameworks. *ACS Catal.* **2013**, *3*, 647−654.

(5) Cao, X.; Chen, Z.; Lin, R.; Cheong, W.-C.; Liu, S.; Zhang, J.; Peng, Q.; Chen, C.; Han, T.; Tong, X.; Wang, Y.; Shen, R.; Zhu, W.; Wang, D.; Li, Y. A Photochromic Composite with Enhanced Carrier Separation for the Photocatalytic Activation of Benzylic C−H Bonds in Toluene. *Nat. Catal.* **2018**, *1*, 704−710.

(6) Cook, T. R.; Zheng, Y.-R.; Stang, P. J. Metal-Organic Frameworks and Self-Assembled Supramolecular Coordination Complexes: Comparing and Contrasting the Design, Synthesis, and Functionality of Metal-Organic Materials. *Chem. Rev.* **2013**, *113*, 734−777.

(7) Furukawa, H.; Cordova, K. E.; O'Keeffe, M.; Yaghi, O. M. The Chemistry and Applications of Metal-Organic Frameworks. *Science* **2013**, *341*, 1230444.

(8) Zhou, H.-C.; Kitagawa, S. Metal-Organic Frameworks (MOFs). *Chem. Soc. Rev.* **2014**, *43*, 5415−5418.

(9) Islamoglu, T.; Goswami, S.; Li, Z.; Howarth, A. J.; Farha, O. K.; Hupp, J. T. Postsynthetic Tuning of Metal-Organic Frameworks for Targeted Applications. *Acc. Chem. Res.* **2017**, *50*, 805−813.

(10) Li, B.; Wen, H.-M.; Cui, Y.; Zhou, W.; Qian, G.; Chen, B. Emerging Multifunctional Metal-Organic Framework Materials. *Adv. Mater.* **2016**, *28*, 8819−8860.

(11) Yang, X.; Sun, J.-K.; Kitta, M.; Pang, H.; Xu, Q. Encapsulating Highly Catalytically Active Metal Nanoclusters inside Porous Organic Cages. *Nat.Catal.* **2018**, *1*, 214−220.

(12) Li, J.; Jiang, L.; Chen, S.; Kirchon, A.; Li, B.; Li, Y.; Zhou, H.-C. Metal-Organic Framework Containing Planar Metal-Binding Sites: Efficiently and Cost-Effectively Enhancing the Kinetic Separation of C_2H_2/C_2H_4. *J. Am. Chem. Soc.* **2019**, *141*, 3807−3811.

(13) Wang, Y.; Zhao, X.; Yang, H.; Bu, X.; Wang, Y.; Jia, X.; Li, J.; Feng, P. A Tale of Two Trimers from Two Different Worlds: A COF-Inspired Synthetic Strategy for Pore-Space Partitioning of MOFs. *Angew. Chem., Int. Ed.* **2019**, *58*, 6316−6320.

(14) Kalmutzki, M. J.; Hanikel, N.; Yaghi, O. M. Secondary Building Units as the Turning Point in the Development of the Reticular Chemistry of MOFs. *Sci. Adv.* **2018**, *4*, eaat9180.

(15) Pattengale, B.; Yang, S.; Ludwig, J.; Huang, Z.; Zhang, X.; Huang, J. Exceptionally Long-Lived Charge Separated State in Zeolitic Imidazolate Framework: Implication for Photocatalytic Applications. *J. Am. Chem. Soc.* **2016**, *138*, 8072−8075.

(16) Dhakshinamoorthy, A.; Asiri, A. M.; García, H. Metal-Organic Framework (MOF) Compounds: Photocatalysts for Redox Reactions and Solar Fuel Production. *Angew. Chem., Int. Ed.* **2016**, *55*, 5414−5445.

(17) Xu, C.; Liu, H.; Li, D.; Su, J.-H.; Jiang, H.-L. Direct Evidence of Charge Separation in a Metal-Organic Framework: Efficient and Selective Photocatalytic Oxidative Coupling of Amines via Charge and Energy Transfer. *Chem. Sci.* **2018**, *9*, 3152−3158.

(18) Zhang, T.; Lin, W. Metal-Organic Frameworks for Artificial Photosynthesis and Photocatalysis. *Chem. Soc. Rev.* **2014**, *43*, 5982−5993.

(19) Xiao, J.-D.; Jiang, H.-L. Metal-Organic Frameworks for Photocatalysis and Photothermal Catalysis. *Acc. Chem. Res.* **2019**, *52*, 356−366.

(20) Li, N.; Liu, J.; Liu, J.-J.; Dong, L.-Z.; Xin, Z.-F.; Teng, Y.-L.; Lan, Y.-Q. Adenine Components in Biomimetic Metal-Organic Frameworks for Efficient CO_2 Photoconversion. *Angew. Chem., Int. Ed.* **2019**, *58*, 5226−5231.

(21) Fu, Y.; Sun, D.; Chen, Y.; Huang, R.; Ding, Z.; Fu, X.; Li, Z. An Amine-Functionalized Titanium Metal-Organic Framework Photocatalyst with Visible-Light-Induced Activity for CO_2 Reduction. *Angew. Chem., Int. Ed.* **2012**, *51*, 3364−3367.

(22) Zhang, H.; Wei, J.; Dong, J.; Liu, G.; Shi, L.; An, P.; Zhao, G.; Kong, J.; Wang, X.; Meng, X.; Zhang, J.; Ye, J. Efficient Visible-Light-Driven Carbon Dioxide Reduction by a Single-Atom Implanted Metal-Organic Framework. *Angew. Chem., Int. Ed.* **2016**, *55*, 14310−14314.

(23) Yuan, S.; Qin, J.-S.; Xu, H.-Q.; Su, J.; Rossi, D.; Chen, Y.; Zhang, L.; Lollar, C.; Wang, Q.; Jiang, H.-L.; Son, D. H.; Xu, H.; Huang, Z.; Zou, X.; Zhou, H.-C. $[Ti_8Zr_2O_{12}(COO)_{16}]$ Cluster: An Ideal Inorganic Building Unit for Photoactive Metal-Organic Frameworks. *ACS Cent. Sci.* **2018**, *4*, 105−111.

(24) Kim, D.; Whang, D. R.; Park, S. Y. Self-Healing of Molecular Catalyst and Photosensitizer on Metal-Organic Framework: Robust Molecular System for Photocatalytic H_2 Evolution from Water. *J. Am. Chem. Soc.* **2016**, *138*, 8698−8701.

(25) Liu, H.; Xu, C.; Li, D.; Jiang, H.-L. Photocatalytic Hydrogen Production Coupled with Selective Benzylamine Oxidation over MOF Composites. *Angew. Chem., Int. Ed.* **2018**, *57*, 5379−5383.

(26) Wu, P.; He, C.; Wang, J.; Peng, X.; Li, X.; An, Y.; Duan, C. Photoactive Chiral Metal-Organic Frameworks for Light-Driven Asymmetric alpha-Alkylation of Aldehydes. *J. Am. Chem. Soc.* **2012**, *134*, 14991−14999.

(27) Zhang, Y.; Guo, J.; Shi, L.; Zhu, Y.; Hou, K.; Zheng, Y.; Tang, Z. Tunable Chiral Metal Organic Frameworks toward Visible Light-Driven Asymmetric Catalysis. *Sci. Adv.* **2017**, *3*, e1701162.

(28) Dhakshinamoorthy, A.; Li, Z.; García, H. Catalysis and Photocatalysis by Metal Organic Frameworks. *Chem. Soc. Rev.* **2018**, *47*, 8134−8172.

(29) Deng, X.; Li, Z.; García, H. Visible Light Induced Organic Transformations Using Metal-Organic-Frameworks (MOFs). *Chem. - Eur. J.* **2017**, *23*, 11189−11209.

(30) Paille, G.; Gomez-Mingot, M.; Roch-Marchal, C.; Lassalle-Kaiser, B.; Mialane, P.; Fontecave, M.; Mellot-Draznieks, C.; Dolbecq, A. A Fully Noble Metal-Free Photosystem Based on Cobalt-Polyoxometalates Immobilized in a Porphyrinic Metal-Organic Framework for Water Oxidation. *J. Am. Chem. Soc.* **2018**, *140*, 3613−3618.

(31) Han, J.; Wang, D.; Du, Y.; Xi, S.; Hong, J.; Yin, S.; Chen, Z.; Zhou, T.; Xu, R. Metal-Organic Framework Immobilized Cobalt Oxide Nanoparticles for Efficient Photocatalytic Water Oxidation. *J. Mater. Chem. A* **2015**, *3*, 20607−20613.

(32) An, Y.; Liu, Y.; An, P.; Dong, J.; Xu, B.; Dai, Y.; Qin, X.; Zhang, X.; Whangbo, M.-H.; Huang, B. Ni^{II} Coordination to an Al-Based Metal-Organic Framework Made from 2-Aminoterephthalate for Photocatalytic Overall Water Splitting. *Angew. Chem., Int. Ed.* **2017**, *56*, 3036−3040.

(33) Lin, W.; Frei, H. Photochemical CO_2 Splitting by Metal-to-Metal Charge-Transfer Excitation in Mesoporous ZrCu(I)-MCM-41 Silicate Sieve. *J. Am. Chem. Soc.* **2005**, *127*, 1610−1611.

(34) Nakamura, R.; Okamoto, A.; Osawa, H.; Irie, H.; Hashimoto, K. Design of All-Inorganic Molecular-Based Photocatalysts Sensitive to Visible Light: Ti(IV)-O-Ce(III) Bimetallic Assemblies on Mesoporous Silica. *J. Am. Chem. Soc.* **2007**, *129*, 9596−9597.

(35) Dvoranová, D.; Barbieriková, Z.; Brezová, V. Radical Intermediates in Photoinduced Reactions on TiO_2 (An EPR Spin Trapping Study). *Molecules* **2014**, *19*, 17279−17304.

(36) Dai, Z.; Qin, F.; Zhao, H. P.; Ding, J.; Liu, Y. L.; Chen, R. Crystal Defect Engineering of Aurivillius Bi_2MoO_6 by Ce Doping for Increased Reactive Species Production in Photocatalysis. *ACS Catal.* **2016**, *6*, 3180−3192.

(37) Nosaka, Y.; Nosaka, A. Y. Generation and Detection of Reactive Oxygen Species in Photocatalysis. *Chem. Rev.* **2017**, *117*, 11302−11336.

(38) Manna, K.; Ji, P.; Lin, Z.; Greene, F. X.; Urban, A.; Thacker, N. C.; Lin, W. Chemoselective Single-Site Earth-Abundant Metal Catalysts at Metal-Organic Framework Nodes. *Nat. Commun.* **2016**, *7*, 12610.

(39) Wang, X.; Zhang, X.; Li, P.; Otake, K.-i.; Cui, Y.; Lyu, J.; Krzyaniak, M. D.; Zhang, Y.; Li, Z.; Liu, J.; Buru, C. T.; Islamoglu, T.; Wasielewski, M. R.; Li, Z.; Farha, O. M. Vanadium Catalyst on Isostructural Transition Metal, Lanthanide, and Actinide Based Metal-Organic Frameworks for Alcohol Oxidation. *J. Am. Chem. Soc.* **2019**, *141*, 8306−8314.

(40) Abdel-Mageed, A. M.; Rungtaweevoranit, B.; Parlinska-Wojtan, M.; Pei, X.; Yaghi, O. M.; Behm, R. J. Highly Active and Stable Single-Atom Cu Catalysts Supported by a Metal-Organic Framework. *J. Am. Chem. Soc.* **2019**, *141*, 5201−5210.

(41) Paglia, G.; Božin, E. S.; Vengust, D.; Mihailovic, D.; Billinge, S. J. L. Accurate Structure Determination of $Mo_6S_yI_z$ Nanowires from Atomic Pair Distribution Function (PDF) Analysis. *Chem. Mater.* **2006**, *18*, 100−106.

(42) White, C. E.; Provis, J. L.; Proffen, T.; Riley, D. P.; van Deventer, J. S. J. Combining Density Functional Theory (DFT) and Pair Distribution Function (PDF) Analysis to Solve the Structure of Metastable Materials: The Case of Metakaolin. *Phys. Chem. Chem. Phys.* **2010**, *12*, 3239−3245.

(43) Schwarz, H. A.; Dodson, R. W. Equilibrium between Hydroxyl Radicals and Thallium (II) and the Oxidation Potential of Hydroxyl (aq). *J. Phys. Chem.* **1984**, *88*, 3643−3647.

(44) Shi, W.; Cao, L.; Zhang, H.; Zhou, X.; An, B.; Lin, Z.; Dai, R.; Li, J.; Wang, C.; Lin, W. Surface Modification of Two-Dimensional Metal-Organic Layers Creates Biomimetic Catalytic Microenvironments for Selective Oxidation. *Angew. Chem., Int. Ed.* **2017**, *56*, 9704−9709.

(45) Kumar, M. S.; Schwidder, M.; Grünert, W.; Brückner, A. On the Nature of Different Iron Sites and Their Catalytic Role in Fe-ZSM-5 DeNOx Catalysts: New Insights by a Combined EPR and UV/VIS Spectroscopic Approach. *J. Catal.* **2004**, *227*, 384−397.

(46) Carter, E.; Carley, A. F.; Murphy, D. M. Evidence for O_2^- Radical Stabilization at Surface Oxygen Vacancies on Polycrystalline TiO_2. *J. Phys. Chem. C* **2007**, *111*, 10630−10638.

(47) Long, J.; Wang, S.; Ding, Z.; Wang, S.; Zhou, Y.; Huang, L.; Wang, X. Amine-Functionalized Zirconium Metal Organic Framework as Efficient Visible-Light Photocatalyst for Aerobic Organic Transformations. *Chem. Commun.* **2012**, *48*, 11656−11658.

(48) Sun, D.; Ye, L.; Li, Z. Visible-Light-Assisted Aerobic Photocatalytic Oxidation of Amines to Imines over NH_2-MIL-125 (Ti). *Appl. Catal., B* **2015**, *164*, 428−432.

(49) Sun, D.; Liu, W.; Qiu, M.; Zhang, Y.; Li, Z. Introduction of a Mediator for Enhancing Photocatalytic Performance via Post-Synthetic Metal Exchange in Metal-Organic Frameworks (MOFs). *Chem. Commun.* **2015**, *51*, 2056−2059.

(50) Lee, Y.; Kim, S.; Kang, J. K.; Cohen, S. M. Photocatalytic CO_2 Reduction by a Mixed Metal (Zr/Ti), Mixed Ligand Metal-Organic Framework under Visible Light Irradiation. *Chem. Commun.* **2015**, *51*, 5735−5738.

(51) Wang, H.; Jiang, S.; Shao, W.; Zhang, X.; Chen, S.; Sun, X.; Zhang, Q.; Luo, Y.; Xie, Y. Optically Switchable Photocatalysis in Ultrathin Black Phosphorus Nanosheets. *J. Am. Chem. Soc.* **2018**, *140*, 3474−3480.

(52) Liu, P.; Zhao, Y.; Qin, R.; Mo, S.; Chen, G.; Gu, L.; Chevrier, D. M.; Zhang, P.; Guo, Q.; Zang, D.; Wu, B; Fu, G.; Zheng, N. Photochemical Route for Synthesizing Atomically Dispersed Palladium Catalysts. *Science* **2016**, *352*, 797−800.

(53) Mirica, L. M.; McCusker, K. P.; Munos, J. W.; Liu, H.-w.; Klinman, J. P. ^{18}O Kinetic Isotope Effects in Non-Heme Iron Enzymes: Probing the Nature of Fe/O_2 Intermediates. *J. Am. Chem. Soc.* **2008**, *130*, 8122−8123.

(54) Li, H.; Qin, F.; Yang, Z.; Cui, X.; Wang, J.; Zhang, L. New Reaction Pathway Induced by Plasmon for Selective Benzyl Alcohol Oxidation on BiOCl Possessing Oxygen Vacancies. *J. Am. Chem. Soc.* **2017**, *139*, 3513−3521.

(55) Oloo, W. N.; Fielding, A. J.; Que, L. Rate-Determining Water-Assisted O-O Bond Cleavage of an Fe^{III}-OOH Intermediate in a Bio-inspired Nonheme Iron-Catalyzed Oxidation. *J. Am. Chem. Soc.* **2013**, *135*, 6438−6441.

(56) Suh, I.; Zhang, R.; Molina, L. T.; Molina, M. J. Oxidation Mechanism of Aromatic Peroxy and Bicyclic Radicals from OH-Toluene Reactions. *J. Am. Chem. Soc.* **2003**, *125*, 12655−12665.

(57) Guo, C.-C.; Liu, Q.; Wang, X.-T.; Hu, H.-Y. Selective Liquid Phase Oxidation of Toluene with Air. *Appl. Catal., A* **2005**, *282*, 55−59.